Flow recession behavior of preferential subsurface flow patterns with minimum energy dissipation

Jannick Strüven[1] and Stefan Hergarten[1]

[1]Institut für Geo- und Umweltnaturwissenschaften, Albertstr. 23B, 79104 Freiburg, Germany

Correspondence: Jannick Strüven
(jannick.strueven@geologie.uni-freiburg.de)

Abstract. Understanding the properties of preferential flow patters is a major challenge in subsurface hydrology. Most of the theoretical approaches in this field stem from research on karst aquifers, where typically two or three distinct flow components with different time scales are considered. This study starts from a different concept, where a continuous spatial variation in transmissivity and storavity over several orders of magnitude is assumed. Distribution and spatial pattern of these properties are derived from the concept of minimum energy dissipation. While the numerical simulation of such systems is challenging, it is found that a reduction to a dendritic flow pattern, similar to rivers at the surface, works well. It is also shown that spectral theory can allow for investigating the fundamental properties of such aquifers. As a main result, the long-term recession of the spring draining the aquifer during periods of drought becomes slower for large catchments. However, the dependence of the respective recession coefficient on catchment size is much weaker than for homogeneous aquifers. Concerning the short-term behavior after an instantaneous recharge event, strong deviations from the exponential recession of a linear reservoir are observed. In particular, it takes a considerable time span until the spring discharge reaches its peak. This rise time is in an order of magnitude of one-seventh of the e-folding recession time. Despite the strong deviations from the linear reservoir at short times, the exponential component typically contributes more than 80 % to the total discharge. This fraction is much higher than expected for karst aquifers and even exceeds the fraction predicted for homogeneous aquifers.

1 Introduction

The recession of spring discharge after recharge events can be seen as the fingerprint of an aquifer. In contrast to pumping tests at wells, it is a passive method based on data that are often recorded routinely. Additionally, spring discharges depend on the overall properties of the catchment, while pumping tests reflect the properties in a region around the well.

More than a century ago, Maillet (1905) suggested the linear reservoir where discharge Q is directly proportional to the stored volume V,

$$Q(t) = \alpha V(t). \tag{1}$$

The linear reservoir is described by a single parameter α [s^{-1}] and the stored volume follows the ordinary differential equation

$$\frac{d}{dt}V(t) = -Q(t) + R(t) = -\alpha V(t) + R(t), \tag{2}$$

25 where $R(t)$ [m^{3}s^{-1}] is the recharge. During periods with zero recharge, both the stored volume and the discharge decay exponentially with the same decay constant α, also called recession coefficient,

$$V(t) \quad = \quad V(0)e^{-\alpha t}, \tag{3}$$
$$Q(t) \quad = \quad Q(0)e^{-\alpha t}. \tag{4}$$

The inverse of the recession coefficient, $\tau = \frac{1}{\alpha}$, defines the e-folding time, so the time interval over which the discharge
30 decreases by a factor of e.

The linear reservoir is not only appealing because it can be described by a single parameter, but even more because its behavior during periods of drought depends only on the actual amount of water, but is independent of the recharge history. It often provides a reasonable approximation for long periods of drought. Deviations from the exponential decay at shorter time scales have been investigated and used for characterizing aquifers since the 1960s, where in particular karst systems have been
35 addressed in numerous studies and several theoretical concepts were proposed.

Forkasiewicz and Paloc (1967) suggested a superposition of three distinct linear reservoirs with different decay constants describing three major flow components – a network of highly conductive conduits, an intermediate system of well integrated fissures, and a network of pores or narrow fissures with low permeability. The behavior of this model is dominated by the slowest reservoir during long periods of drought.
40 A different approach using two components was suggested by Mangin (1975). The slow component was described as a linear reservoir, and a fast component with a limited range was added. The parameters of the fast components are the basis of the widely used karst classification system suggested in the same study. Several other modeling approaches which are similar in their spirit were developed (e.g., Drogue, 1972; Atkinson, 1977; Padilla et al., 1994; Kovács and Perrochet, 2014; Xu et al., 2018; Basha, 2020; Kovács, 2021). Beyond these approaches, a multitude of numerical models designed for simulating real-
45 world scenarios is nowadays availaible. For deeper insights, readers are referred to the review paper by Fiorillo (2014) and to the model comparison by Jeannin et al. (2021).

While deviations from the linear reservoir are particular relevant for karst systems, it should be noted that even the simplest Darcy-type aquifers are not linear reservoirs. Assuming a given transmissivity T [m^{2}s^{-1}] and a given storavity S [-], the simplest Darcy-type aquifer is described by the water balance equation

50 $$S\frac{\partial h}{\partial t} = -\mathrm{div}\boldsymbol{q} + r, \tag{5}$$

where h [m] is the hydraulic head,

$$\boldsymbol{q} = -T\nabla h, \tag{6}$$

[m^{2}s^{-1}] the 2-D flux density (volume per time and cross section width), ∇ the 2-D gradient operator, r the recharge per area [ms^{-1}], and div the 2-D divergence operator. Inserting Eq. (6) into Eq. (5) yields a partial differential equation of the diffusion type for the hydraulic head h,

$$S\frac{\partial h}{\partial t} = \mathrm{div}\,(T\nabla h) + r. \tag{7}$$

This model was investigated in several studies for constant T and S in square or rectangular domains (e.g., Rorabaugh, 1964; Nutbrown, 1975; Kovács et al., 2005; Kovács and Perrochet, 2008). Applying spectral theory (see Sect. 2.3), it was shown that the total discharge Q (q integrated over the entire boundary) can be described by an infinite series of exponential terms with different decay constants during periods of drought. Since the term with the smallest decay constant dominates at large times, the behavior approaches that of the linear reservoir. However, the question how well the linear reservoir approximates the properties of real aquifers practically or whether the linear reservoir is even some kind of preferred state from a theoretical point of view, has been discussed controversially (e.g., Fenicia et al., 2006; de Rooij, 2014; Kleidon and Savenije, 2017; Savenije, 2018).

Including the early recession phase in the analysis yields more information about the aquifer, but increases the dependence of the results on the recharge history in turn. The instantaneous unit hydrograph, which dates back to concepts of Sherman (1932), is widely used in this context. It describes the discharge arising from a unit amount of recharge that is applied instantaneously at $t = 0$ over the entire domain.

The unit hydrograph of the simple Darcy aquifer differs strongly from that of the linear reservoir and as well as from the empirical approaches proposed by Forkasiewicz and Paloc (1967) and by Mangin (1975). While these models predict a finite discharge at $t = 0$, it diverges according to a power law,

$$Q(t) \propto t^{-\frac{1}{2}}, \tag{8}$$

in the limit $t \to 0$ for the simple Darcy aquifer (e.g., Hergarten and Birk, 2007). Such a power-law decrease also occurs in models consisting of porous blocks connected by highly conductive conduits (Kovács et al., 2005; Kovács and Perrochet, 2008). However, a finite conductance of the conduits limits the power-law divergence at short times (Kovács and Perrochet, 2014). Hergarten and Birk (2007) extended this concept by a fractal distribution of block sizes. While this model was able to explain a power-law recession with exponents different from $-\frac{1}{2}$, deriving aquifer properties from the power-law behavior of recession curves turned out to be challenging. Birk and Hergarten (2010) investigated synthetic hydrographs for recharge events of finite duration and found that the properties of the recharge event likely shadow the short-term dynamics of the porous blocks.

This study addresses the influence of preferential flow patterns on hydrograph recession in a more general context. In particular, focus is not explicitly on karst systems. As a major difference towards the studies mentioned above, we do not start from a binary or ternary system of distinct flow components, but assume a continuous variation in the hydraulic properties over several orders of magnitude in combination with a highly organized spatial pattern.

However, the description of heterogeneity and its representation in numerical models is one of the major challenges in hydrology. On the other hand, there seems to be an increasing number of studies attempting to derive preferred stated of the

atmosphere and the hydrosphere from principles of optimality (e.g., Kleidon and Schymanski, 2008; Kleidon and Renner, 2013; Kleidon et al., 2014; Kleidon and Savenije, 2017; Kleidon et al., 2019; Zehe et al., 2010, 2013, 2021; Westhoff and Zehe, 2013; Westhoff et al., 2014, 2017; Zhao et al., 2016). In the context of fluid flow, minimum energy dissipation seems to
90   be a promising concept, which was successfully applied to river networks (Howard, 1990; Rodriguez-Iturbe et al., 1992a, b; Rinaldo et al., 1992; Maritan et al., 1996) and to the cardiovascular system of mammals (West et al., 1997; Enquist et al., 1998, 1999; Banavar et al., 1999; West et al., 1999a, b).

Hergarten et al. (2014) developed a theory for an optimal spatial distribution of porosity and hydraulic conductivity in the sense that the total energy dissipation of the flow is minimized. However, there seem to be neither validations by real-world
95   data nor direct applications of this concept so far. Nevertheless, it seems to be the simplest available scheme for generating highly organized synthetic patterns of porosity and conductivity and will therefore be used in this study.

2   Approach

2.1   Basic setup

In this study, we assume the simplest scenario of a 2-D aquifer with a given transmissivity T [m^{2}s^{-1}] and a given storativity S
100   [-], described by Eqs. (5) and (6). Since focus is on strongly organized preferential flow patterns, both T and S are not constant, but may even vary over several orders of magnitude.

On a regular grid with a uniform grid spacing d, Eqs. (5) and (6) can be discretized by a finite-volume approach according to

$$d^2 S_i \frac{\partial h_i}{\partial t} = - \sum_{j \in N(i)} q_{ij} + d^2 r_i \tag{9}$$

105   with the fluxes

$$q_{ij} = d T_{ij} \frac{h_i - h_j}{d}. \tag{10}$$

The nodes of the grid were numbered by a single index i, where $N(i)$ denotes the nearest neighborhood of the node i, consisting of four neighbors except for boundary nodes. The symbol q_{ij} [m^{2}s^{-1}] refers to the flux from the node i to the node j, while T_{ij} is the respective transmissivity. Note that q_{ij} already includes the length of the edge between the two nodes (first term d in
110   Eq. 10), so that it is no longer a flux per unit width. Inserting Eq. (10) into Eq. (9) yields the respective discrete form of Eq. (7).

Solving this equation numerically on large grids is challenging if the transmissivity varies over several orders of magnitude. Using an explicit scheme for the timestep requires very small time increments since small changes in hydraulic head cause large fluxes. Employing a fully implicit scheme overcomes this limitation since fully implicit schemes are stable at arbitrary time increments for diffusion-type equations. However, most of the available algorithms for solving the resulting linear equation
115   system do not perform well if T varies strongly. This also applies to multigrid schemes (e.g., Hackbusch, 1985), which are the only schemes with linear time complexity, so where the numerical effort per time step increases only linearly with the number of nodes.

2.2 Dendritic flow patterns

In the theory of minimum energy dissipation in Darcy flow proposed by Hergarten et al. (2014), preferential flow patterns
120 are approximated by dendritic structures. This means that each node i delivers its entire discharge to one of its neighbors, b, called flow target in the following (strictly speaking, it should be labeled b_i). The flow target is defined as the neighbor with the steepest descent in hydraulic head h, which is the same as the neighbor with the lowest h for a grid with uniform spacing in both directions. Then, the neighborhood consists of three groups of nodes: (i) One flow target. (ii) Some neighbors that deliver their discharge to the considered node, called donors in the following. (iii) Some nodes that do not interact with the considered
125 node. The last group of nodes makes the difference towards the original model where all neighbored nodes interact.

The discrete version of the balance equation (Eq. 9) turns into

$$d^2 S_i \frac{\partial h_i}{\partial t} = -q_i + \sum_{j \in D(i)} q_j + d^2 r_i \qquad (11)$$

for a dendritic flow pattern, where the notation q_i (with a single index) describes the flux from the node i to its flow target (so q_{ib} in the general notation). The sum extends over all donors of the node i, denoted $D(i)$ here.

130 Dendritic networks are widely used in the context of surface flow patterns, in particular river networks at large scales. In order to reduce effects of anisotropy, the so-called D8 scheme is typically used. Here, 8 neighbors (4 nearest neighbors and 4 diagonal neighbors) are considered, so that river segments are either parallel to one of the coordinate axes or diagonal. While the numerical construction of optimized drainage patters by Hergarten et al. (2014) also used the D8 scheme, we consider only the 4 nearest neighbors (D4 scheme) in the following. The main reason for this limitation is the comparison to the original
135 model in Sect. 3.1. The D4 scheme can be seen as a restriction of the original model, while the D8 version would allow for additional flow paths. In particular, a diagonal line of points with a high transmissivity would be a preferential flow path with regard to the D8 scheme, but not in the original model.

While the concept of dendritic flow patterns was used by Hergarten et al. (2014) for constructing patterns of porosity and conductivity (see also Sect. 2.5), recent developments in numerics make this concept interesting for time-dependent modeling.
140 In the following section, a numerical scheme is presented which overcomes the numerical limitations arising from strong variations in transmissivity for dendritic flow patterns.

2.3 Spectral theory

Large parts of this study are based on spectral theory. Spectral theory decomposes the solution into a set of functions with a simple behavior. For diffusion problems, these are functions that decay through time exponentially. For the continuous problem
145 (Eq. 7), this means that we look for functions $h(\boldsymbol{x}, t)$ with the property

$$h(\boldsymbol{x}, t) = h(\boldsymbol{x}, 0) e^{-\alpha t}, \qquad (12)$$

for zero recharge ($r = 0$), where α is the decay constant. Inserting Eq. (12) into Eq. (7) (for $r = 0$) yields

$$-\frac{1}{S} \text{div}(T \nabla h) = \alpha h. \qquad (13)$$

This means that the function $h(\boldsymbol{x},0)$ (and thus also $h(\boldsymbol{x},t)$) must be an eigenfunction of the differential operator $-\frac{1}{S}\mathrm{div}T\nabla$ at
150 the left-hand side of Eq. (13), where α is the respective eigenvalue.

While the eigenfunctions and the respective eigenvalues can be computed analytically for some simple geometries (e.g., Rorabaugh, 1964; Nutbrown, 1975; Kovács et al., 2005; Kovács and Perrochet, 2008, for rectangular domains) and constant parameters, a heterogeneous distribution of S and T requires a numerical treatment. Using the same finite volume discretization as above, the differential operator $-\frac{1}{S}\mathrm{div}T\nabla$ can be written in matrix form

$$155 \quad -\frac{1}{S}\mathrm{div}\left(T\nabla h\right) \,\widehat{=}\, Ah, \tag{14}$$

where h at the right-hand side is a vector consisting of all head values h_i and A is a square matrix. Assuming unit grid spacing ($d=1$) for simplicity, the nondiagonal elements of the matrix are

$$A_{ij} = \begin{cases} -\frac{T_{ij}}{S_i} & \text{for } j \in N(i) \\ 0 & \text{else} \end{cases}, \tag{15}$$

while the diagonal elements are

$$160 \quad A_{ii} = \sum_{j\in N(i)} \left(-A_{ij}\right) = \sum_{j\in N(i)} \frac{T_{ij}}{S_i}. \tag{16}$$

The respective form of the matrix for dendritic flow patterns is basically the same, where only the neighborhood has to be reduced to those points that are connected, i.e., where either j is the flow target of i or vice versa.

The prerequisite for applying spectral theory is that each initial distribution of hydraulic head values can be written as a linear combination of eigenvectors (discrete representations of eigenfunctions on the grid) in the form

$$165 \quad h_i(0) = \sum_k \lambda_k e_{ki}, \tag{17}$$

with coefficients λ_k, where e_{ki} is the i-th component of the k-th eigenvector (so the k-th eigenfunction evaluated at the node i). Then the hydraulic heads at time t are

$$h_i(t) = \sum_k \lambda_k e_{ki} e^{-\alpha_k t} \tag{18}$$

if the recharge is zero for all t, where α_k is the k-th eigenvalue of A. So all head values and thus also all fluxes can be written
170 as a sum of exponentially decaying terms. In particular, the discharge of a spring can be decomposed into a sum of exponential functions,

$$Q(t) = \sum_k \lambda_k Q_k e^{-\alpha_k t}, \tag{19}$$

where Q_k is the discharge of the k-th eigenfunction. If we assume that the eigenvalues are sorted in increasing order, the long-term recession coefficient is $\alpha = \alpha_1$.

If the matrix A is symmetric, even an orthonormal basis of eigenvectors exists, so that a representation according to Eqs. (17) and (18) is possible. Since $T_{ij} = T_{ji}$, the matrix A is symmetric if the storavity S_i is the same at all nodes, but symmetry is broken for a spatially variable storavity. This problem can be fixed by defining a specific inner product instead of the standard scalar product. While the latter is

$$h \cdot \tilde{h} = \sum_i h_i \tilde{h}_i \tag{20}$$

for any h and $\tilde{h}$, we define

$$h \cdot \tilde{h} = \sum_i S_i h_i \tilde{h}_i. \tag{21}$$

Using the definition of A (Eqs. 15 and 16), it is easily recognized that

$$S_i A_{ij} = S_j A_{ji}, \tag{22}$$

and thus

$$
\begin{aligned}
(Ah) \cdot \tilde{h} &= \sum_i S_i \left(\sum_j A_{ij} h_j \right) \tilde{h}_i && (23)\\
&= \sum_{i,j} S_i A_{ij} h_j \tilde{h}_i && (24)\\
&= \sum_{i,j} S_j A_{ji} h_j \tilde{h}_i && (25)\\
&= \sum_{i,j} S_j h_j \left(\sum_i A_{ji} \tilde{h}_i \right) && (26)\\
&= h \cdot \left(A\tilde{h} \right). && (27)
\end{aligned}
$$

This is the condition for the symmetry of A with regard to the new inner product. So the eigenvectors e_k of A are orthogonal, and an orthonormal basis is obtained by normalizing them in such a way that

$$e_k \cdot e_k = \sum_i S_i e_{ki}^2 = 1. \tag{28}$$

If h_i are the head values at $t = 0$, the coefficients λ_k in Eqs. (17) and (18) are obtained by

$$\lambda_k = h \cdot e_k = \sum_i S_i h_i e_{ki}. \tag{29}$$

This relation becomes particularly simple for the instantaneous unit hydrograph since $S_i h_i = 1$ for all nodes here, and thus

$$\lambda_k = \sum_i e_{ki}. \tag{30}$$

2.4 Forward modeling

Since computing the instantaneous unit hydrograph at short times requires a large number of eigenfunctions for big catchments, we also implemented a numerical scheme for forward modeling of the dendritic model. For this purpose, we adopted the very

200 efficient, fully implicit scheme that was recently proposed in the context of fluvial erosion and sediment transport by Hergarten (2020). For simplicity, the scheme is only described for the D4 neighborhood with unit grid spacing ($d = 1$) in the following.

Let us consider a time step from t to $t + \delta t$. Replacing the time derivative at the left-hand side of Eq. (11) by a difference quotient and evaluating the fluxes at the right-hand side at the time $t + \delta t$ (for the fully implicit treatment) yields

$$S_i \frac{h_i(t+\delta t) - h_i(t)}{\delta t} = -q_i(t+\delta t) + \sum_{j \in D(i)} q_j(t+\delta t) + r_i. \tag{31}$$

205 The key idea behind the scheme is that all fluxes respond linearly to baselevel changes due to the linearity of the differential equation. In particular, the flux $q_i(t+\delta t)$ depends linearly on the head value of its flow target b, so that

$$q_i(t+\delta t) = q_i^0 + q_i'\left(h_b(t+\delta t) - h_b(t)\right). \tag{32}$$

Here, q_i^0 is the flux at time $t+\delta t$ if the baselevel remains constant, i.e., $h_b(t+\delta t) = h_b(t)$ (so not $q_i(t)$), while q_i' is the derivative of $q_i(t+\delta t)$ with respect to the baselevel $h_b(t+\delta t)$.

210 As shown in Appendix A, q_i^0 and q_i' can be computed from the respective properties of the donors and from the known values of h at time t by the expressions

$$q_i^0 = T_i \frac{\left(\frac{S_i}{\delta t} - \sum_j q_j'\right)(h_i(t) - h_b(t)) + \sum_j q_j^0 + r_i}{\frac{S_i}{\delta t} + T_i - \sum_j q_j'}, \tag{33}$$

$$q_i' = -T_i \frac{\frac{S_i}{\delta t} - \sum_j q_j'}{\frac{S_i}{\delta t} + T_i - \sum_j q_j'}. \tag{34}$$

Thus, q_i^0 and q_i' can be computed successively in downstream order, starting from the nodes without donors.

215 Once the values q_j^0 and q_j' have been computed, the values $h_i(t+\delta t)$ and the respective fluxes $q_i(t+\delta t)$ are computed in a second sweep over the grid. This sweep works in upstream direction, starting from the boundary of the domain. As soon as the head value $h_b(t+\delta t)$ of the flow target is known, Eq. (32) can be used for computing the flux $q_i(t+\delta t)$ from the considered node. Finally, the hydraulic head can be calculated from Eq. (10) according to

$$h_i(t+\delta t) = h_b(t+\delta t) + \frac{q_i(t+\delta t)}{T_i}. \tag{35}$$

220 This scheme provides a direct solver (without the need for iterations) for the fully implicit discretization of the flow equation on a dendritic network. It is therefore stable for arbitrary time increments δt, and its performance is not affected by spatial variations in transmissivity and storativity. The numerical complexity is $O(n)$, which means the the computing effort increases only linearly with the total number of nodes. It is therefore perfectly suited for simulations on grids with several millions of nodes.

2.5 Patterns of transmissivity and storavity

While systematic knowledge about the spatial structure of preferential flow paths is still limited, we need a model for generating spatial patterns of transmissivity and storavity. In this study, we adopt the theory based on minimum energy dissipation proposed by Hergarten et al. (2014). This theory addresses the best spatial distribution of a given total pore space volume in the sense that the total energy dissipation of steady-state flow is minimized. Assuming a power-law dependence of the hydraulic conductivity K on the porosity ϕ,

$$K \propto \phi^n \tag{36}$$

with a given exponent n, it was found that K and ϕ must depend on the volumetric flux density (Darcy velocity) q in the form

$$\phi \quad \propto \quad q^{\frac{2}{n+1}}, \tag{37}$$
$$K \quad \propto \quad q^{\frac{2n}{n+1}}. \tag{38}$$

Hergarten et al. (2014) computed optimized dendritic networks on a discrete grid based on these relations. For simplicity, we assume that Eq. (37) also holds for the storavity and Eq. (38) for the transmissivity, both with q as the flux per unit width.

Assuming a steady state with uniform recharge, the flux per unit with can be replaced by the respective catchment size A. For convenience, we define the grid spacing as the length scale of the system and thus measure A in grid pixels. In addition, we set the factors of proportionality to unity, so that

$$S_i \quad = \quad A_i^{\frac{2}{n+1}}, \tag{39}$$
$$T_i \quad = \quad A_i^{\frac{2n}{n+1}}. \tag{40}$$

Practically, setting the factors of proportionality to unity defines a nondimensional time scale in addition to the spatial scale. According to Eqs. (10) and (11), the smallest spatial unit (a single-pixel catchment) is described by the equation

$$d^2 S_i \frac{\partial h_i}{\partial t} = -T_i (h_i - h_b) \tag{41}$$

for zero recharge. So the smallest spatial units behave like a linear reservoir with a recession coefficient

$$\alpha = \frac{T_i}{d^2 S_i} = 1, \tag{42}$$

which means that one nondimensional time unit is the characteristic time of a single-pixel element.

2.6 Considered scenarios

Based on the assumptions described in the previous section, a numerically obtained flow pattern for $n = 2$ on a 4096×4096 grid is used in this study. Points at the boundaries are considered as springs where the discharge is measured. Figure 1 illustrates the catchments of the springs.
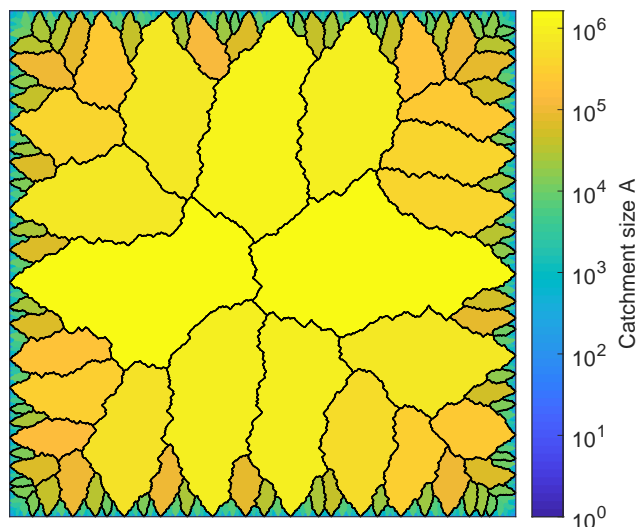
Figure 1. Catchments of numerically obtained dendritic flow patterns for $n = 2$ on a lattice of 4096×4096 sites. Color corresponds to the size A of each individual catchment, measured in grid pixels. The watersheds between large catchments ($A \geq 10000$ pixels) are highlighted in black.

Several scenarios will be considered for the same geometry in the following. Beside the reference scenario with $n = 2$, the influence of n will be investigated. These investigations also include uniform transmissivity and storativity. The suitability of the description as a dendritic network will be tested against full Darcy flow.

In order to enable a comparison of the recession curves of individual springs, the same catchments are used in all simulations. This means that the boundaries between the catchments shown in Fig. 1 are enforced by cutting the respective connections, so by inhibiting flow across the watersheds.

3 Results

3.1 Dendritic flow patterns vs. full Darcy flow

As a first step, we investigate under which conditions the reduction from full Darcy flow (taking all four neighbors into account) to a dendritic flow pattern (a single flow target for each node) provides a suitable approximation. We start from the optimized distribution of S and T for $n = 2$, so from a strongly preferential flow pattern. Figure 2 compares the long-term recession coefficients α (α_1 in Eq. 19) obtained from the dendritic flow pattern to those of full Darcy flow. The recession coefficients of both approaches agree well, which means that the long-term recession behavior is captured well by the dendritic flow pattern. Some deviations occur at rather small catchment sizes from about 10 to 200. Here, allowing only one single flow direction leads to a slight underestimation of α. This underestimation is highest at catchment sizes $A \approx 16$ and reaches about 10 % there.
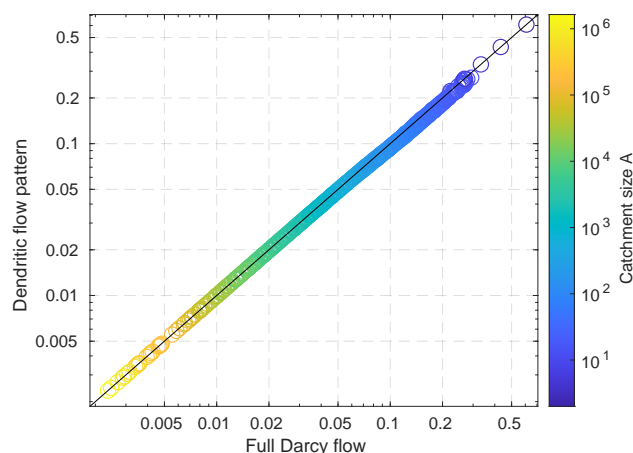
Figure 2. Recession coefficient α of each individual catchment with $n = 2$ for dendritic flow patterns against full Darcy flow. The colors match Fig. 1 and indicate the size of the respective catchment.

While a slower recession (a decrease in α) is the expected behavior when restricting the flow pattern to certain directions, it may be surprising at first that the effect vanishes for very small catchments. However, we have to keep in mind that we used a subdivision into predefined catchments. So nodes at drainage divides between two catchments are already restricted concerning their drainage directions for the full Darcy flow scenario.

In order to investigate the effect of the restricted flow directions in more detail, we analyzed the flow pattern of the full Darcy scenario. For this purpose, we define the major flux component of each node as the flux towards the given flow target (according to the dendritic pattern) and the minor flux component as the sum of the fluxes towards all other neighbors with lower head values.

Figure 3 shows the relative contribution of the minor fluxes as a function of the size of the respective upstream catchment size. The upstream catchment size refers to the individual pixels here and not to the embedding catchment. So the data point for a $A = 1$ describes the average over all pixels without donors, no matter whether they are draining directly to the boundary (so are indeed single-pixel catchments) or are part of a larger catchment. In order to avoid artifacts arising from the restricted flow directions at drainage divides, inner points and points at drainage divides were investigated separately.

The contribution of the minor fluxes decreases with increasing catchment size, so downstream along the preferential flow paths. It becomes negligible for all considered scenarios at catchment sizes $A \gtrsim 200$. The contribution of the minor flux is particularly small immediately after a short, uniform recharge pulse. This result is owing to the relation between transmissivity and storavity. The initial distribution of the head values is inverse to the storavity, which is high along preferential flow paths. So there are strong gradients in hydraulic head from sites with small catchment sizes towards sites with large catchment sizes, which focus the fluxes towards the preferential flow paths.

The strongest contribution of the minor fluxes is found for the long-term recession, characterized by an exponential recession curve. The minor fluxes contribute even almost 60 % for $A = 1$ here (only inner points, about 35 % for drainage divides). It
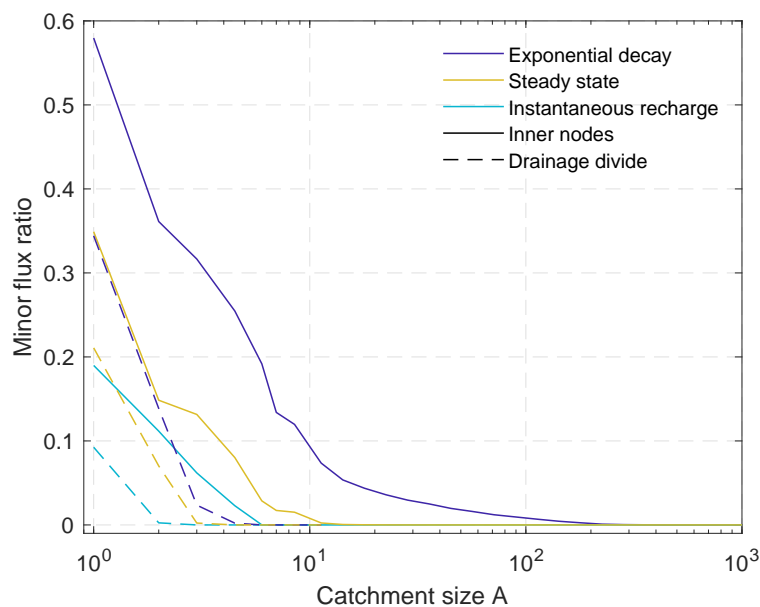
Figure 3. Relative contribution of the minor fluxes for each grid pixel as a function of their respective catchment size A. The curves were obtained by logarithmic binning with ten bins per decade. All three considered scenarios, a steady-state initial condition, a unit recharge pulse, and the exponentially decaying term are separated into grid pixels that lie within a spring catchment (flow between all four neighbors; solid lines) and pixels at drainage divides (restricted flow directions; dashed lines).

may be surprising that the minor fluxes do not affect the recession coefficient strongly, as shown in Fig. 2. In an extreme scenario where all four neighbors are at the same head values, the fluxes would be four times higher in the full Darcy model than in the single flow target realization, which would result in a four times faster recession than predicted by Eq. 42. Although

290 the majority of the nodes have small upstream catchment sizes (e.g., $A = 1$ for 43 % of all nodes and $A \leq 10$ for 81 % of all nodes), their behavior is obviously not crucial for the properties of the entire catchment.

These results suggest preferential flow patterns can be represented well on a discrete grid by a dendritic structure where each node drains only towards one of its neighbors. In turn, the approximation by a dendritic flow pattern does not work well for a

295 spatially uniform distribution of T and S as shown in Fig. 4. Here, α is underestimated by more than one order of magnitude for large catchments, which means that the recession is more than by a factor of 10 too slow. The coefficients agree well only for small catchments, where the minor fluxes are small or even absent due to the restricted flow directions at drainage divides.

3.2 Scaling properties of the recession coefficient

It was already visible in Figs. 2 and 4 that the recession coefficient α decreases with increasing catchment size. The scaling

300 behavior expected from Eq. (7) is $\alpha \propto A^{-1}$, which arises from the first-order time derivative at the left-hand side and the second-order spatial derivatives at the right-hand side. If we rescale the entire catchment including the pattern of S and T by a
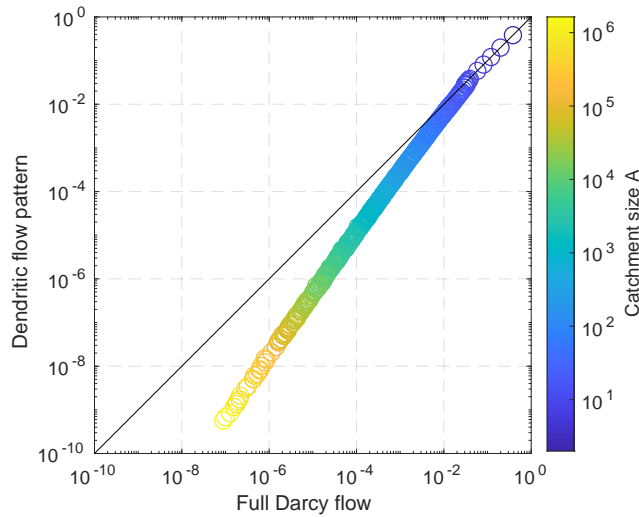
Figure 4. Recession coefficient α of each individual catchment with a spatially uniform distribution of T and S for dendritic flow patterns against full Darcy flow. The colors match Fig. 1 and indicate the size of the respective catchment.

factor β, the right-hand side of Eq. (7) changes by a factor of β^{-2}. Then the time scale must change by the same factor. Since the catchment size A increases quadratically with β, the time scale is proportional to the catchment size and thus $\alpha \propto A^{-1}$.

As shown in Fig. 5, this simple scaling behavior does not hold for the patterns of S and T considered here. While the scaling behavior follows a power law

$$\alpha \propto A^{-\gamma} \tag{43}$$

reasonably well for all considered values of n, it seems that an exponent $\gamma = 1$ is only achieved for $n = 1$. For all values $n > 1$, we find $\gamma < 1$, where γ decreases with increasing n. This means that the recession of large catchments is still slower than the recession of small catchments, but the effect is considerably weaker than for a simple Darcy-type aquifer ($\gamma = 1$).

Qualitatively, this weaker increase is the expected behavior for a preferential flow pattern. Preferential flow paths are able to transport water rapidly over large distances, so that an increasing spatial extension does not slow down the recession as it would be the case for a homogeneous aquifer.

The opposite behavior is observed for $n < 1$. Here large catchments become extremely slow. Revisiting Eqs. (39) and (40), it is recognized that T still increases with catchment size, but weaker than S for $n < 1$. So flow is still facilitated along the preferential flow paths, but the respective cells become slow due to their high storavity. This becomes visible if we apply Eq. (42) formally to such cells, which yields $\alpha \propto A^{\frac{2(n-1)}{n+1}}$, so that α decreases with increasing A. However, $n < 1$ would be unrealistic for porous media, where rather $n \geq 2$ should be expected. Beyond this, it was demonstrated by Hergarten et al. (2014) that dendritic flow patterns are energetically favorable only for $n > 1$. So preferential flow patterns with $n < 1$ can be constructed, but do not make much sense. Nevertheless, the curves are almost indistinguishable not only for $n \geq 1$, but also for $n < 1$. The results reveal that the numerical approximation by a dendritic flow pattern also works well for $n < 1$.
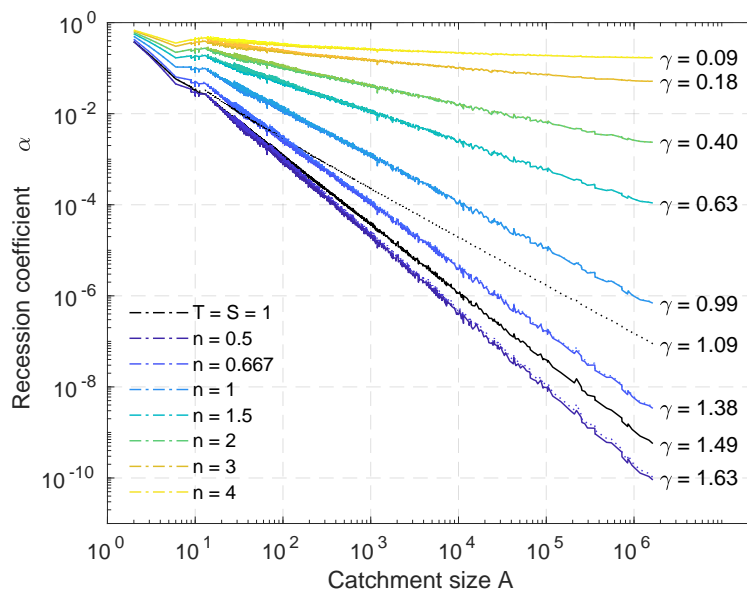
Figure 5. Scaling behavior of recession coefficient α relating to catchment size A (Eq. 43) for different values of n and for a uniform distribution of T and S. Full Darcy flow is plotted as solid lines, flow in dendritic patterns as dotted lines. Except for the scenario with $S = T = 1$, the curves of full Darcy flow and the dendritic pattern are hardly distinguishable.

As already recognized in Sect. 3.1, the approximation by a dendritic flow pattern does not work for constant transmissivity and storavity. Figure 5 reveals that the unusual scaling behavior with $\gamma > 1$ also occurs for the description by full Darcy flow. This result is related to the subdivision of the domain into fixed catchments drained by distinct springs. In order to test this hypothesis, we computed the recession coefficients for radial flow towards a spring in polar coordinates. Keeping the radius
325   of the spring constant and varying the total size of the catchment (the outer radius), we obtained roughly the same scaling behavior, $\gamma \approx 1.1$, as found for the catchments considered in Fig. 5. This scaling behavior indicates that the region around the spring is some kind of bottleneck that becomes increasingly relevant for large catchments. This result aligns well with the result of Hergarten et al. (2014), who found that minimum energy dissipation for radial flow requires an increase in permeability towards the spring.

330   ## 3.3   Short-term recession

The differences between the model considered here and simple Darcy-type models are not limited to the scaling properties of the long-term recession coefficient. As exemplified in Fig. 6 for the biggest catchment, the unit hydrograph shows a clear rising limb at short times. In contrast, the 1-D Darcy-type aquifer shows a power-law decrease in discharge at short times, so that $Q \rightarrow \infty$ for $t \rightarrow 0$.
335   For a better comparison, size and parameter values of the 1-D aquifer were adjusted in such a way that the long-term recession coefficient α and the total amount of water are the same as for the considered catchment (see Appendix B). For such
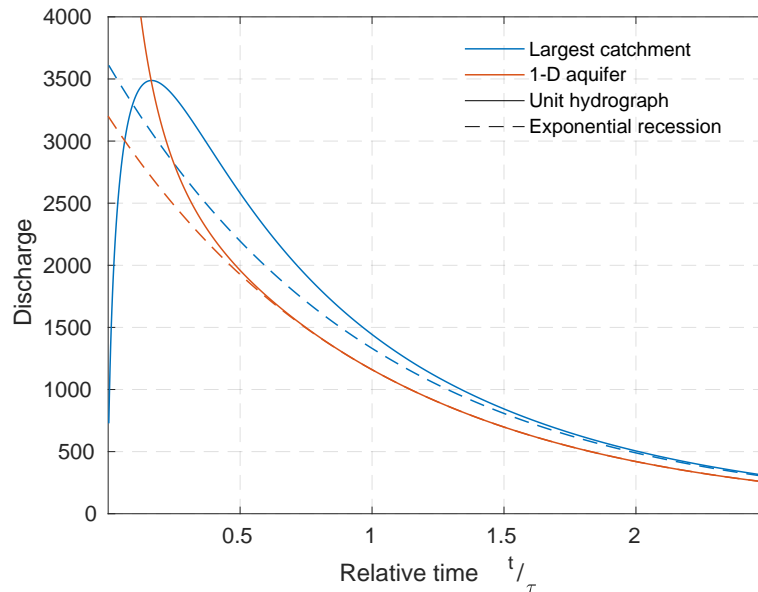
Figure 6. Unit hydrographs of the biggest catchment for $n = 2$ and of a homogeneous 1-D aquifer. The dashed lines correspond to the long-term exponential recession. The data are scaled in such a way that the e-folding time τ and the total amount of water are the same in both scenarios.

a simple aquifer, a lag between a short precipitation event and the peak discharge would typically be attributed to the infiltration process. We would then assume that the time lag is related to the transit time of the water from the surface to the aquifer. In a model consisting of individual porous blocks connected by highly conductive fractures (e.g., Kovács et al., 2005; Hergarten

340 and Birk, 2007), the time lag may also be owing to the finite conductivity of the fracture system. In contrast, the finite rise time is an inherent property of the structure of the aquifer in the model considered here. It cannot be attributed uniquely to any individual component of the system.

Figure 7 provides an analysis of the rise time t_{rise} for the considered catchments and different values of the exponent n. For $n = 2$, the data suggest a linear relationship between t_{rise} and the long-term e-folding time $\tau = \frac{1}{\alpha}$. The ratio of t_{rise} and τ varies

345 from about 9 % to 19 % for the individual catchments. The rise times become slightly shorter in relation to the e-folding time for lower n. For $n = 1.5$, we found ratios in a range from about 4 % to 22 %. The data obtained for $n > 2$ are non-unique, in particular for small catchments (small τ). Overall, there seems to be a weak increase in the ratio of t_{rise} and τ with increasing n. This trend aligns well with the absence of a finite rise time in the simple one- and two-dimensional aquifers without a preferential flow pattern. However, the trend is much weaker than the variation among individual catchments and therefore not

350 investigated further. In each case, however, t_{rise} is not very small compared to τ. One-seventh of the e-folding recession time seems to be a reasonable order of magnitude. Taking into account that long-term e-folding times of karst aquifers are typically in an order of magnitude of several weeks, the rise time is in an order of magnitude of several days.
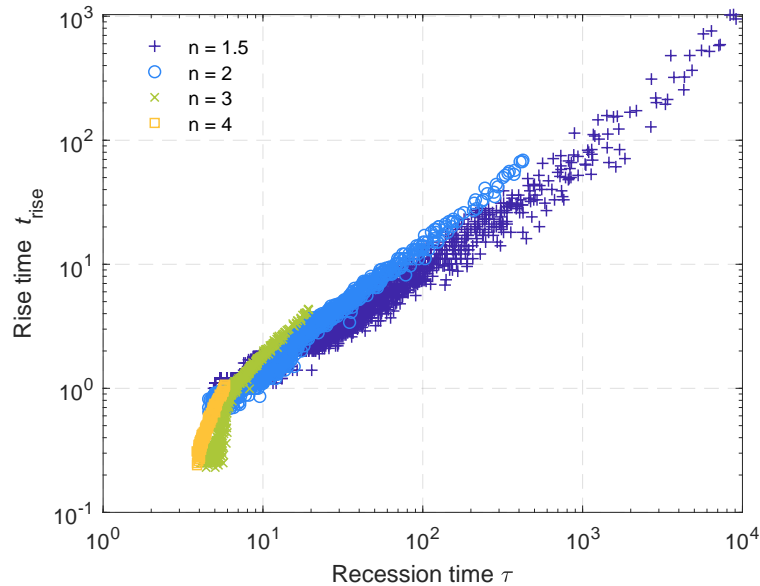
Figure 7. Relation between rise time t_{rise} and e-folding time τ of the long-term recession for the considered catchments and different values of n.

The occurrence of a rising limb in the unit hydrograph requires that some of the coefficients $\lambda_k Q_k$ in Eq. (19) are negative. This can be seen formally by computing the derivative of Eq. (19). The derivatitve is similar to Eq. (19) itself, except that the coefficients are $-\alpha_k \lambda_k Q_k$. Since the sum cannot become zero if all coefficients have the same sign, at least one of the original coefficients $\lambda_k Q_k$ must be negative. Figure 8 shows the coefficients for the largest catchment. While the coefficients of the slowest components (small α_k) are positive, there is no obvious preference for either sign in the faster components.

The spectrum of the considered catchment differs fundamentally from that of the 1-D aquifer. While the spectrum of the 1-D aquifer consists of distinct components with recession coefficients $\alpha_k \propto (2k-1)^2$ (see Appendix B), the spectrum of the catchment becomes more or less continuous at large k. However, the smallest recession coefficients are still distinct. For the catchment analyzed in Fig. 8, the ratio is $\frac{\alpha_2}{\alpha_1} \approx 2$. While the lowest ratios among all simulated catchments are about 1.5, the ratio is typically in a range from about 2.5 to 4 for smaller catchments. So the ratio $\frac{\alpha_2}{\alpha_1}$ differs from catchment to catchment, but is always clearly above unity (also for $n \neq 2$). This property ensures that the recession curve approaches a single exponential function at a reasonable time and that the coefficient $\lambda_1 Q_1$ captures the long-term recession well. However, the ratio is much lower than $\frac{\alpha_2}{\alpha_1} = 9$ for the 1-D aquifer. Although the deviation from an exponential recession also depends on the coefficients $\lambda_k Q_k$, the difference is already visible in Fig. 6. While the unit hydrograph of the 1-D aquifer is almost indistinguishable from the exponential decay at $t = 0.5\tau$, the difference is more than 15 % at this time for the largest catchment. So the model with the preferential flow pattern approaches the long-term exponential recession much more slowly than the simple 1-D aquifer.

Figure 9 illustrates the approximation of the unit hydrograph by a finite number of exponential components. In this example, all coefficients for $k \leq 9$ are positive. In the range $9 < k \leq 23$, there are also negative coefficients. However, the positive
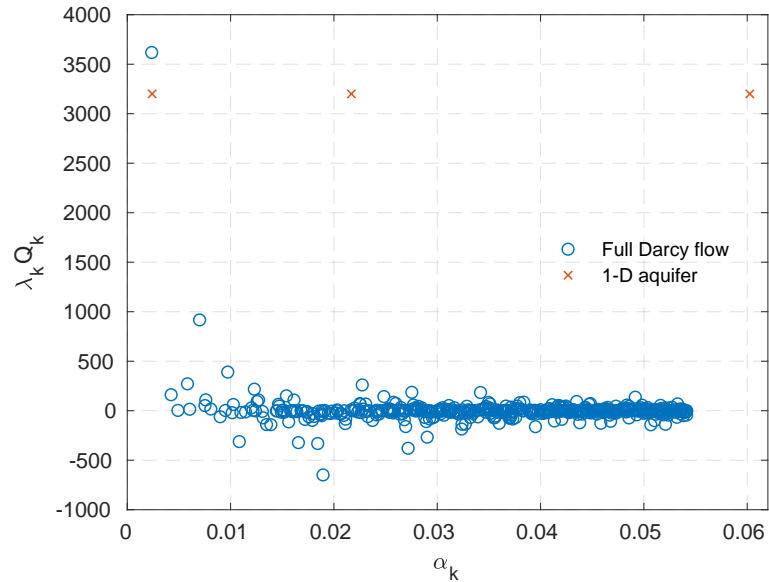
Figure 8. Coefficients $\lambda_k Q_k$ and recession coefficients α_k in Eq. (19) for the largest catchment ($n = 2$). Only the slowest 500 components ($k \leq 500$) were computed. The data of the 1-D aquifer were rescaled in such a way that the lowest recession coefficient α_1 and the total discharge are the same as for the simulated catchment.

coefficients still dominate here, so that the highest peak discharge is achieved when including the components with $k \leq 23$. The negative components become increasingly relevant for larger k. This results in a decreasing peak discharge, however, still at $t = 0$ for $k \leq 60$. The component with $k = 61$ is the first that shifts the peak discharge to a time $t > 0$ an thus produces a rising limb in the unit hydrograph. However, approximating the behavior around the peak discharge reasonably well requires
375 several hundred components.

The occurrence of negative coefficients in Eq. (19) is not a principal problem, but impedes a simple interpretation of the decomposition into exponentially decreasing terms. If all components were positive, we could imagine the aquifer as a set of linear reservoirs drained in parallel. However, negative components would correspond to reservoirs with a negative amount of water. Formally, the slow component (first exponential function) could even contain more water than available in total, and
380 the fast components (all higher exponentials) could be negative in total. In Fig. 6, this would mean that the area of the unit hydrograph below the exponential component at short times was larger than the area above the exponential component. In this case, the widely used characterization of karst aquifers by the contribution of the slow (exponential) component to the total discharge (Mangin, 1975; Jeannin and Sauter, 1998) would be taken at absurdum.

Figure 10 shows the contribution of the slow component (first exponential) to the total amount of water for all catchments
385 considered here ($n = 2$). Depending on the catchment size, this contribution is between 77 % and 104 %. So there are indeed catchments where the effect of the rising limb is so strong that the slow component is formally larger than the total recharge
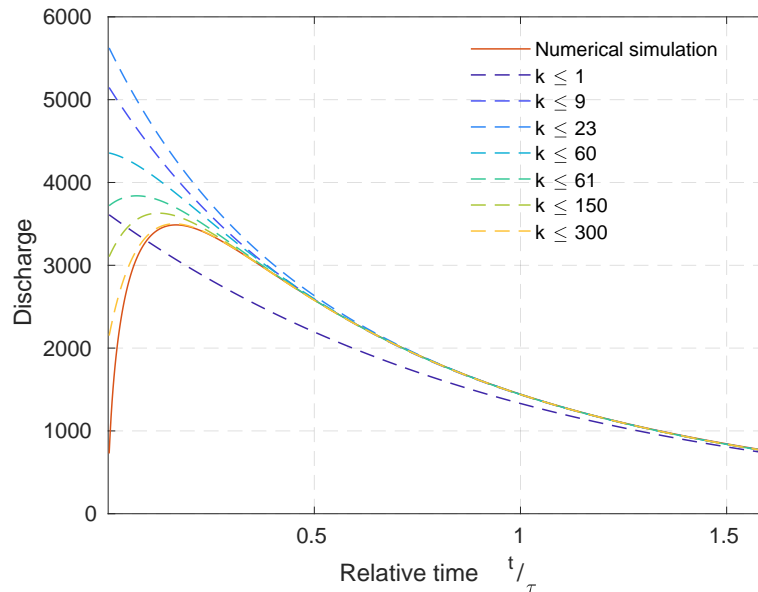
Figure 9. Recession curves of the largest catchment obtained from the numerical simulation and different numbers of exponential functions (Eq. 19).

and the fast components are negative in sum. However, this effect is found only for some rather small catchments. For the largest catchments, the contribution of the slow component is about 90 %.

The obtained contributions of the slow component are high compared to other models. For the 1-D aquifer used here as a
390 reference, this contribution is $\frac{8}{\pi^2} \approx 81$ %. For an aquifer consisting of square porous blocks connected by conduits with infinite conductance, it is $\frac{64}{\pi^4} \approx 66$ % (e.g., Birk and Hergarten, 2010). The contribution of the slow component was not explicitly investigated by Hergarten and Birk (2007) in their fractal model with power-law distributed block sizes. However, since the slowest flow component arises from the largest blocks, the total contribution of the slow component must even be considerably smaller than the 66 % obtained for an aquifer with a uniform block size. In the widely used classification scheme of karst
395 aquifers proposed by Mangin (1975), even aquifers with a contribution of the slow component of less than 50 % are considered poorly karstified (see also Jeannin and Sauter, 1998). So our continuous model of preferential flow patterns predicts even a higher contribution of the slow component to the unit hydrograph than other models and is far off from what is typically assumed for karst systems.

At first sight, the observed high contribution of the slow component could be an effect of the finite rise time. As recognized in
400 Figs. 6 and 9, the unit hydrograph is below the slow component for $t \lessgtr 0.5 t_{\mathrm{rise}}$. When investigating recession curves in reality, the analysis typically starts from the peak in discharge ($t = t_{\mathrm{rise}}$). The orange-colored markers in Fig. 10 show the respective contributions of the slow component. Starting the analysis from $t = t_{\mathrm{rise}}$ instead of $t = 0$ indeed yields lower contributions of the slow components. However, the effect is only in an order of magnitude of a few percent. So the result that continuous preferential flow patterns predict a high contribution of the slowest flow component is not an artifact of the analysis.
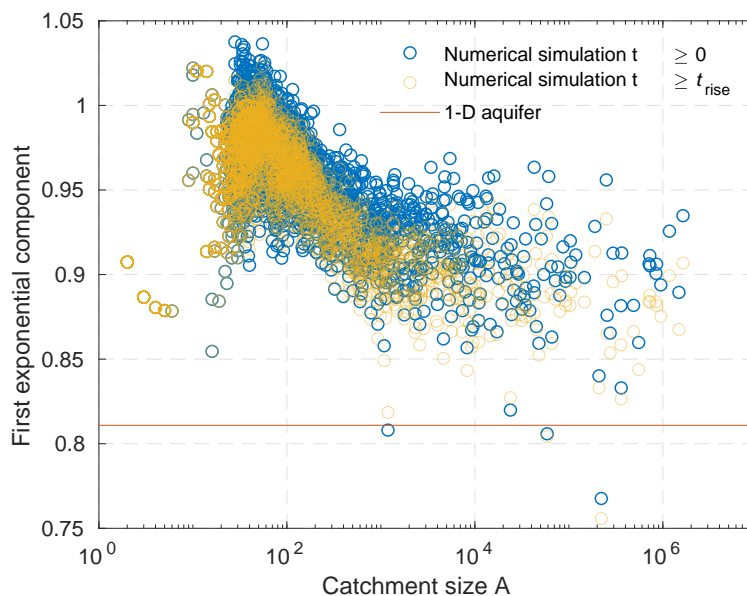
Figure 10. Contribution of the slowest exponential component to the total discharge for the considered catchments. The red line shows the respective contribution of $\frac{8}{\pi^2} \approx 81\,\%$ for the 1-D aquifer.

3.4 The effect of non-uniform recharge

While the unit hydrograph describes uniform recharge, the spatial distribution of the recharge may have a strong influence on recession curves of large catchments. As a simple example, we separated the domain into a proximal part and a distal part. Both parts are equally sized, and the distinction is made by the distance from the boundary of the domain. Since the overall domain is the same, the recession coefficients α_k of all flow components are the same as for the entire domain. Only the coefficients a_k in Eq. (19) differ. This difference, however, has a strong effect on the rise time and on the contribution of the slow flow component.

Figure 11 compares the results obtained numerically for the largest catchments to those obtained by spectral decomposition for a 1-D aquifer (for details, see Appendix B). While a completely filled 1-D aquifer starts with a peak at $t = 0$, applying recharge only to the distal part of the domain introduces a finite rise time. This rise time is, however, shorter (in relation to the e-folding recession time) than for the aquifer with the preferential flow pattern. The rise time of the preferential flow pattern also changes considerably if recharge is applied only to a part of the domain. The strong influence may be surprising at first since we could expect that the signal propagates rapidly through the preferential flow structure from the distal part of the domain to the spring. However, preferential flow paths have not only a high transmissivity here, but also a high storativity. Thus, the propagation of signals is not as fast as we might expect.

The contribution of the slowest component also changes if only a part of the domain is filled. Similarly to the rise time, it increases if only the distal part of the domain is filled since the instantaneous recharge signal has already been smoothed
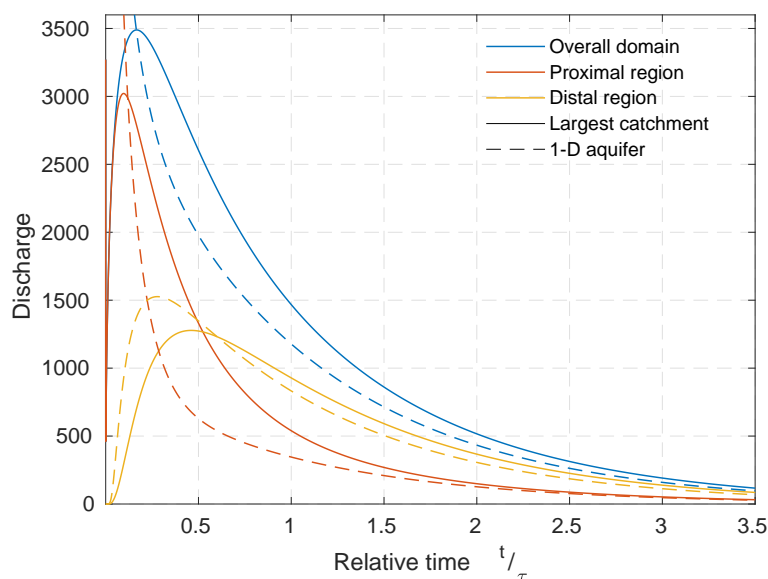
Figure 11. Instantaneous unit hydrographs for partly filled domains. Solid lines refer to the largest catchment of the simulation, and dashed lines to a homogeneous aquifer. The data are scaled in such a way that the e-folding time τ and the total amount of water are the same in both scenarios. Proximal and distal regions cover half of the catchment each.

when it arrives at the spring. The contribution of the first exponential component is formally higher than 100 % for the distal part. For the largest simulated catchment, it is 137 %, while it is 115 % for the 1-D aquifer. In turn, the contribution of the first exponential component is lower for the proximal parts; 50 % for the largest catchment in the simulation and 47 % for the 1-D

425   aquifer. So the contribution of the first exponential component is always higher for the preferential flow pattern than for the 1-D aquifer, and the effect of applying recharge only to a part of the domain is similar.

These results substantiate the relevance of the spatial distribution of the recharge for the short-term recession. The difference between the preferential flow pattern and a homogeneous 1-D aquifer is, however, rather small. It mainly concerns the behavior at very short times, with a finite rise time for the preferential flow pattern and a peak at $t = 0$ for the 1-D aquifer if the recharge

430   is applied to the proximal part of the domain.

4   Conclusions and perspectives

This study is a first attempt to describe the dynamics of aquifers with continuous preferential flow patterns. In contrast to approaches based on two or three distinct flow components widely used in the context of karst aquifers, the concept used here assumes a continuous spatial variation in hydraulic properties over several orders of magnitude.

435   An aquifer with a flat bottom and time-independent transmissivity was considered as the simplest scenario. Synthetic spatial patterns of transmissivity and storativity were obtained from principles of minimum energy dissipation based on the theory proposed by Hergarten et al. (2014).

As a major technical result, it was found that such aquifers can be approximated well by dendritic flow patterns, in which the entire discharge of each cell is delivered to the neighbor with the steepest gradient in hydraulic head. This approximation has been widely used for channelized flow patterns at the surface. The dendritic structure enables an efficient, fully implicit numerical scheme with a numerical effort that increases only linearly with the number of cells, also known as $O(n)$ complexity. This property allows for simulations on grids consisting of several million nodes and thus for a reasonable spatial resolution of the preferential flow pattern.

As a second, rather theoretical result, it was shown that spectral theory is not restricted to homogeneous aquifers, but can also be applied to aquifers with any spatial distribution of transmissivity and storavity. Although the eigenvalues and the respective eigenvectors have to be computed numerically, this approach allows for a fast computation of the long-term recession coefficient without forward modeling over a long time span. In addition, the contribution of the slowest flow component to the instantaneous unit hydrograph (and also to any other initial state) can be computed easily.

The long-term recession coefficient α depends on the catchment size. The dependency is, however, weaker than for homogeneous aquifers and follows a power law $\alpha \propto A^{-\gamma}$ (Eq. 43). The exponent γ depends on the assumed relation between transmissivity T and storavity S. It approaches 1 for $T \propto S$, which is also the limit where dendritic flow patterns are energetically favorable. In this case, the scaling is the same as for homogeneous aquifers ($\gamma = 1$). For relations $T \propto S^n$, γ decreases with increasing n. As a typical value, $\gamma = 0.4$ was found for $n = 2$. So the decrease in the recession coefficient with catchment size is typically less than half as strong as for homogeneous aquifers.

Since flow patterns obtained from minimum energy dissipation are typically scale-invariant, a power-law decrease of the discharge after a short recharge pulse might be expected at first. However, the respective instantaneous unit hydrograph shows a completely different behavior. The discharge immediately after the recharge event is quite small, and it takes a considerable time until it reaches its peak. This rise time is in an order of magnitude of one-seventh of the e-folding recession time ($\tau = \alpha^{-1}$). It seems nor to depend strongly on the catchment size neither on the relation between transmissivity and storavity.

The contribution of the slowest component to the unit hydrograph is in an order of magnitude of 90 % for large catchments and even larger for small catchments. This contribution increases further if recharge is applied only to a part of the domain far away from the spring and even exceeds 100 % then. Formally, this result arises from the occurrence of negative coefficients in decomposition of the unit hydrograph into exponentially decaying components. The occurrence of negative coefficients also inhibits the simple interpretation as a set of linear reservoirs draining in parallel. Measuring the contribution of the slowest component from the peak of the unit hydrograph instead of the time at which the instantaneous recharge occurs reduces the contribution of the slowest component only slightly. This contribution is higher than for homogeneous aquifers and much higher than typically assumed for karst aquifers (less than 50 %).

So we have to conclude that preferential flow patterns arising from a strongly organized pattern of transmissivity and storavity differ fundamentally from karst aquifers in their properties. For future work, it would be interesting to find out whether the difference mainly concerns the contribution of the slowest flow component or also the scaling of the recession coefficient with catchment size.

For the further development, an extension of the numerical scheme towards unconfined sloping aquifers (e.g., Rupp and Selker, 2006; Pauritsch et al., 2015) would be particularly useful. Although there is ongoing development in this field (e.g., Alemie et al., 2019; Pathania et al., 2019), including preferential flow patterns at a reasonable spatial resolution is still a

475 challenge here. Extending the implicit scheme for dendritic flow patterns towards unconfined sloping aquifer would still be challenging, but might considerably contribute to understanding the response of hillslopes to precipitation events and phenomena such as subsurface stormflow (e.g., Chifflard et al., 2019).

Appendix A: The fully implicit scheme for a dendritic network

In this section, Eqs. (33) and (34), which are the basis of the implicit scheme discussed in Sect. 2.4, are proven. Inserting

480 Eqs. (10) and (32) into Eq. (31) yields

$$S_i \frac{h_i(t+\delta t) - h_i(t)}{\delta t} = -T_i \left(h_i(t+\delta t) - h_b(t+\delta t) \right) + \sum_{j \in D(i)} q_j^0 + \sum_{j \in D(i)} q_j' \left(h_i(t+\delta t) - h_i(t) \right) + r_i, \tag{A1}$$

and thus

$$h_i(t+\delta t) - h_i(t) = \frac{T_i \left(h_b(t+\delta t) - h_i(t) \right) + \sum_j q_j^0 + r_i}{\frac{S_i}{\delta t} + T_i - \sum_j q_j'}. \tag{A2}$$

Using Eq. (10), we can then compute the flux according to

485 $$q_i(t+\delta t) = T_i \left(h_i(t+\delta t) - h_b(t+\delta t) \right) \tag{A3}$$

$$= T_i \left(\frac{T_i \left(h_b(t+\delta t) - h_i(t) \right) + \sum_j q_j^0 + r_i}{\frac{S_i}{\delta t} + T_i - \sum_j q_j'} + h_i(t) - h_b(t+\delta t) \right) \tag{A4}$$

$$= T_i \frac{\left(\frac{S_i}{\delta t} - \sum_j q_j' \right) \left(h_i(t) - h_b(t+\delta t) \right) + \sum_j q_j^0 + r_i}{\frac{S_i}{\delta t} + T_i - \sum_j q_j'}. \tag{A5}$$

Then q_i^0 (Eq. 33) is obtained by setting $h_b(t+\delta t) = h_b(t)$ and and q_i' (Eq. 34) by taking the derivative with respect to $h_b(t+\delta t)$.

Appendix B: The unit hydrograph of a homogeneous 1-D aquifer

490 Let us consider a 1-D aquifer with a length L, where the spring is located at $x = 0$ and the drainage divide at $x = L$. Then the boundary conditions are $h(x,t) = 0$ at $x = 0$ and $\frac{\partial}{\partial x} h(x,t) = 0$ at $x = L$, and $h(x,t)$ is periodic with a wavelength of $4L$. Thus, $h(x,0)$ can be written as a Fourier series

$$h(x,0) = \sum_{k=1}^{\infty} a_k \sin \left(\frac{2\pi k x}{4L} \right), \tag{B1}$$

where the respective terms with the cosine function are zero due to the boundary conditions and $a_k = 0$ for even values of k.

495 The coefficients a_k are given by the relation

$$a_k = \frac{2}{4L} \int_0^{4L} h(x,0) \sin \left(\frac{2\pi k x}{4L} \right) dx = \frac{2}{L} \int_0^L h(x,0) \sin \left(\frac{2\pi k x}{4L} \right) dx. \tag{B2}$$

If we assume that the distal region, $\lambda L \leq x \leq L$ with $\lambda \in [0, 1]$, is initially filled to a given head value h_0, we obtain

$$a_k = \frac{2h_0}{L} \int_{\lambda L}^{L} \sin\left(\frac{2\pi k x}{4L}\right) dx = \frac{4h_0}{\pi k} \cos\left(\frac{\pi k \lambda}{2}\right) \tag{B3}$$

for uneven values of k. The time-dependent solution $h(x,t)$ must satisfy the 1-D version of Eq. (7) with $r = 0$,

500 $$S \frac{\partial h}{\partial t} = \frac{\partial}{\partial x}\left(T \frac{\partial h}{\partial x}\right). \tag{B4}$$

It is easily recognized that the solution of this equation with the initial condition defined by Eq. (B1) is

$$h(x,t) = \sum_{k=1}^{\infty} a_k \sin\left(\frac{2\pi k x}{4L}\right) e^{-\alpha_k t}, \tag{B5}$$

where

$$\alpha_k = \frac{T}{S}\left(\frac{\pi k}{2L}\right)^2. \tag{B6}$$

505 Then the flux per unit width across the boundary is

$$q(t) = T \left.\frac{\partial}{\partial x} h(x,t)\right|_{x=0} = T \sum_{k=1}^{\infty} a_k \frac{2\pi k}{4L} e^{-\alpha_k t} = \frac{2Th_0}{L} \sum_{\substack{k=1 \\ (\text{uneven})}}^{\infty} \cos\left(\frac{\pi k \lambda}{2}\right) e^{-\alpha_k t} \tag{B7}$$

with the coefficients a_k from Eq. (B3). The respective expression for the proximal region, $0 \leq x \leq \lambda L$, is readily obtained by subtracting this expression from the same expression with $\lambda = 0$.

Code and data availability. All codes and simulated data are available in a Zenodo repository at https://doi.org/10.5281/zenodo.7050521
510 (Strüven, 2022). The authors are happy to assist interested readers in reproducing the results and performing subsequent research.

Author contributions. J.S. developed the numerical codes and analyzed the results. S.H. developed the theoretical framework. Both authors wrote the paper.

Competing interests. The authors declare that there is no conflict of interest.

Acknowledgements. This work was funded by the Deutsche Forschungsgemeinschaft (DFG, German Research Foundation) – 414728598.

515 **References**

Alemie, T. C., Tilahun, S. A., Ochoa-Tocachi, B. F., Schmitter, P., Buytaert, W., Parlange, J.-Y., and Steenhuis, T. S.: Predicting shallow groundwater tables for sloping highland aquifers, Water Resour. Res., 55, 11 088–11 100, https://doi.org/10.1029/2019WR025050, 2019.

Atkinson, T. C.: Diffuse flow and conduit flow in limestone terrain in the Mendip Hills, Sommerset (Great Britain), J. Hydrol., 35, 93–110, https://doi.org/10.1016/0022-1694(77)90079-8, 1977.

520 Banavar, J. R., Maritan, A., and Rinaldo, A.: Size and form in efficient transportation networks, Nature, 399, 130–132, https://doi.org/10.1038/20144, 1999.

Basha, H. A.: Flow recession equations for karst systems, Water Resour. Res., 56, e2020WR027 384, https://doi.org/10.1029/2020WR027384, 2020.

Birk, S. and Hergarten, S.: Early recession behaviour of spring hydrographs, J. Hydrol., 387, 24–32, 525 https://doi.org/10.1016/j.jhydrol.2010.03.026, 2010.

Chifflard, P., Blume, T., Maerker, K., Hopp, L., van Meerveld, I., Graef, T., Gronz, O., Hartmann, A., Kohl, B., Martini, E., Reinhardt-Imjela, C., Reiss, M., Rinderer, M., and Achleitner, S.: How can we model subsurface stormflow at the catchment scale if we cannot measure it?, Hydrol. Process., 33, 1378–1385, https://doi.org/0.1002/hyp.13407, 2019.

de Rooij, G. H.: Is the groundwater reservoir linear? A mathematical analysis of two limiting cases, Hydrol. Earth Syst. Sci. Discuss., 11, 530 83–108, https://doi.org/10.5194/hessd-11-83-2014, 2014.

Drogue, C.: Analyse statistique des hydrogrammes de decrues des sources karstiques, J. Hydrol., 15, 49–68, https://doi.org/10.1016/0022-1694(72)90075-3, 1972.

Enquist, B. J., Brown, J. H., and West, G. B.: Allometric scaling of plant energetics and population density, Nature, 395, 163–165, https://doi.org/10.1038/25977, 1998.

535 Enquist, B. J., West, G. B., Charnov, E. L., and Brown, J. H.: Allometric scaling of production and life-history variation in vascular plants, Nature, 401, 907–911, https://doi.org/10.1038/44819, 1999.

Fenicia, F., Savenije, H. H. G., Matgen, P., and Pfister, L.: Is the groundwater reservoir linear? Learning from data in hydrological modelling, Hydrol. Earth Syst. Sci., 10, 139–150, https://doi.org/10.5194/hess-10-139-2006, 2006.

Fiorillo, F.: The recession of spring hydrographs, focused on karst aquifers, Water Resour. Manage., 28, 1781–1805, 540 https://doi.org/10.1007/s11269-014-0597-z, 2014.

Forkasiewicz, J. and Paloc, H.: Le régime de tarissement de la Foux-de-la-Vis. Etude préliminaire., Chron. hydrogéol., 3, 61–73, 1967.

Hackbusch, W.: Multi-Grid Methods and Applications, Springer, Berlin, Heidelberg, New York, https://doi.org/10.1007/978-3-662-02427-0, 1985.

Hergarten, S.: Transport-limited fluvial erosion – simple formulation and efficient numerical treatment, Earth Surf. Dynam., 8, 841–854, 545 https://doi.org/10.5194/esurf-8-841-2020, 2020.

Hergarten, S. and Birk, S.: A fractal approach to the recession of spring hydrographs, Geophys. Res. Lett., 34, 11 401, https://doi.org/10.1029/2007GL030097, 2007.

Hergarten, S., Winkler, G., and Birk, S.: Transferring the concept of minimum energy dissipation from river networks to subsurface flow patterns, Hydrol. Earth Syst. Sci., 18, 4277–4288, https://doi.org/10.5194/hess-18-4277-2014, 2014.

550 Howard, A. D.: Theoretical model of optimal drainage networks, Water Resour. Res., 26, 2107–2117, https://doi.org/10.1029/WR026i009p02107, 1990.

Jeannin, P.-Y. and Sauter, M.: Analysis of karst hydrodynamic behaviour using global approaches: a review, Bull. Hydrogeol., 16, 31–48, 1998.

Jeannin, P.-Y., Artigue, G., Butscher, C., Chang, Y., Charlier, J.-B., Duran, L., Gill, L., Hartmann, A., Johannet, A., Jourde, H., Kavousi, A., Liesch, T., Liu, Y., Lüthi, M., Malard, A., Mazzilli, N., Pardo-Igúzquiza, E., Thiéry, D., Reimann, T., Schuler, P., Wöhling, T., and Wunsch, A.: Karst modelling challenge 1: Results of hydrological modelling, J. Hydrol., 600, 126 508, https://doi.org/10.1016/j.jhydrol.2021.126508, 2021.

Kleidon, A. and Renner, M.: Thermodynamic limits of hydrologic cycling within the Earth system: concepts, estimates and implications, Hydrol. Earth Syst. Sci., 17, 2873–2892, https://doi.org/10.5194/hess-17-2873-2013, 2013.

Kleidon, A. and Savenije, H. H. G.: Minimum dissipation of potential energy by groundwater outflow results in a simple linear catchment reservoir, Hydrol. Earth Syst. Sci. Discuss. (preprint), 2017, 1–11, https://doi.org/10.5194/hess-2017-674, 2017.

Kleidon, A. and Schymanski, S. J.: Thermodynamics and optimality of the water budget on land: a review, Geophys. Res. Lett., 35, L20 404, https://doi.org/10.1029/2008GL035393, 2008.

Kleidon, A., Renner, M., and Porada, P.: Estimates of the climatological land surface energy and water balance derived from maximum convective power, Hydrol. Earth Syst. Sci., 18, 2201–2218, https://doi.org/10.5194/hess-18-2201-2014, 2014.

Kleidon, A., Zehe, E., and Loritz, R.: ESD Ideas: Structures dominate the functioning of Earth systems, but their dynamics are not well represented, Hydrol. Earth Syst. Sci. Discuss., in review, https://doi.org/10.5194/esd-2019-52, 2019.

Kovács, A.: Quantitative classification of carbonate aquifers based on hydrodynamic behaviour, Hydrogeol. J., 29, 33–52, https://doi.org/10.1007/s10040-020-02285-w, 2021.

Kovács, A. and Perrochet, P.: A quantitative approach to spring hydrograph decomposition, J. Hydrol., 352, 16–29, https://doi.org/10.1016/j.jhydrol.2007.12.009, 2008.

Kovács, A. and Perrochet, P.: Well hydrograph analysis for the estimation of hydraulic and geometric parameters of karst and connected water systems, in: H2Karst Research in Limestone Hydrogeology, edited by Mudry, J., Zwahlen, F., Bertrand, C., and LaMoreaux, J., pp. 97–114, Springer, Cham, https://doi.org/10.1007/978-3-319-06139-9_7, 2014.

Kovács, A., Perrochet, P., Király, L., and Jeannin, P.-Y.: A quantitative method for the characterisation of karst aquifers based on spring hydrograph analysis, J. Hydrol., 303, 152–164, https://doi.org/10.1016/j.jhydrol.2004.08.023, 2005.

Maillet, E.: Essais d'Hydraulique souterraine et fluviale, Librairie Scientifique A. Hermann, Paris, 1905.

Mangin, A.: Contribution a l'etude hydrodynamique des aquifères karstiques, Ph.D. thesis, Université de Dijon, 1975.

Maritan, A., Colaiori, F., Flammini, A., Cieplak, M., and Banavar, J. R.: Universality classes of optimal channel networks, Science, 272, 984–986, https://doi.org/10.1126/science.272.5264.984, 1996.

Nutbrown, D. A.: Identification of parameters in a linear equation of groundwater flow, Water Resour. Res., 11, 581–588, https://doi.org/10.1029/WR011i004p00581, 1975.

Padilla, A., Pulido-Bosch, A., and Mangin, A.: Relative importance of baseflow and quickflow from hydrographs of karst spring, Groundwater, 32, 267–277, https://doi.org/10.1111/j.1745-6584.1994.tb00641.x, 1994.

Pathania, T., Bottacin-Busolin, A., Rastogi, A. K., and Eldho, T. I.: Simulation of groundwater flow in an unconfined sloping aquifer using the element-free Galerkin method, Water Resour. Manage., 33, 2827—-2845, https://doi.org/10.1007/s11269-019-02261-4, 2019.

Pauritsch, M., Birk, S., Wagner, T., Hergarten, S., and Winkler, G.: Analytical approximations of discharge recessions for steeply sloping aquifers in alpine catchments, Water Resour. Res., 51, 8729–8740, https://doi.org/10.1002/2015WR017749, 2015.

Rinaldo, A., Rodriguez-Iturbe, I., Bras, R. L., Ijjasz-Vasquez, E., and Marani, A.: Minimum energy and fractal structures of drainage net-
590   works, Water Resour. Res., 28, 2181–2195, https://doi.org/10.1029/92WR00801, 1992.

Rodriguez-Iturbe, I., Rinaldo, A., Rigon, R., Bras, R. L., Ijjasz-Vasquez, E., and Marani, A.: Fractal structures as least energy patterns: The
        case of river networks, Geophys. Res. Lett., 19, 889–892, https://doi.org/10.1029/92GL00938, 1992a.

Rodriguez-Iturbe, I., Rinaldo, A., Rigon, R., Bras, R. L., Marani, A., and Ijjasz-Vasquez, E.: Energy dissipation, runoff production, and the
        three-dimensional structure of river basins, Water Resour. Res., 28, 1095–1103, https://doi.org/10.1029/91WR03034, 1992b.

595 Rorabaugh, M. I.: Estimating changes in bank storage and ground-water contribution to streamflow, IAHS Publication, 63, 432–441, 1964.

Rupp, D. E. and Selker, J. S.: On the use of the Boussinesq equation for interpreting recession hydrographs from sloping aquifers, Water
        Resour. Res., 42, W12 421, https://doi.org/10.1029/2006WR005080, 2006.

Savenije, H. H. G.: HESS Opinions: Linking Darcy's equation to the linear reservoir, Hydrol. Earth Syst. Sci., 22, 1911–1916,
        https://doi.org/10.5194/hess-22-1911-2018, 2018.

600 Sherman, L. K.: Stream flow from rainfall by the unit graph method, Engineering News-Record, 108, 501–505, 1932.

Strüven, J.: Flow recession behavior of preferential subsurface flow patterns, https://doi.org/10.5281/zenodo.7050521, 2022.

West, G. B., Brown, J. H., and Enquist, B. J.: A general model for the origin of allometric scaling laws in biology, Science, 276, 122–126,
        https://doi.org/10.1126/science.276.5309.122, 1997.

West, G. B., Brown, J. H., and Enquist, B. J.: A general model for the structure and allometry of plant vascular systems, Nature, 400, 664–667,
605   https://doi.org/10.1038/23251, 1999a.

West, G. B., Brown, J. H., and Enquist, B. J.: The fourth dimension of life: fractal geometry and allometric scaling of organisms, Science,
        284, 1677–1679, https://doi.org/10.1126/science.284.5420.1677, 1999b.

Westhoff, M. C. and Zehe, E.: Maximum entropy production: can it be used to constrain conceptual hydrological models?, Hydrol. Earth
        Syst. Sci., 17, 3141–3157, https://doi.org/10.5194/hess-17-3141-2013, 2013.

610 Westhoff, M. C., Zehe, E., and Schymanski, S. J.: Importance of temporal variability for hydrological predictions based on the maximum
        entropy production principle, Geophys. Res. Lett., 41, 67–73, https://doi.org/10.1002/2013GL058533, 2014.

Westhoff, M. C., Erpicum, S., Archambeau, P., Pirotton, M., and Dewals, B.: Maximum energy dissipation to explain velocity fields in
        shallow reservoirs, J. Hydraul. Res., https://doi.org/10.1080/00221686.2017.1289268, 2017.

Xu, B., Ye, M., Dong, S., Dai, Z., and Pei, Y.: A new model for simulating spring discharge recession and estimating effective porosity of
615   karst aquifers, J. Hydrol., 562, 609–622, https://doi.org/10.1016/j.jhydrol.2018.05.039, 2018.

Zehe, E., Blume, T., and Blöschl, G.: The principle of maximum energy dissipation: a novel thermodynamic perspective on rapid water flow
        in connected soil structures, Philos. T. Roy. Soc. B, 365, 1377–1386, https://doi.org/10.1098/rstb.2009.0308, 2010.

Zehe, E., Ehret, U., Blume, T., Kleidon, A., Scherer, U., and Westhoff, M.: A thermodynamic approach to link self-organization, preferential
        flow and rainfall–runoff behaviour, Hydrol. Earth Syst. Sci., 17, 4297–4322, https://doi.org/10.5194/hess-17-4297-2013, 2013.

620 Zehe, E., Loritz, R., Edery, Y., and Berkowitz, B.: Preferential pathways for fluid and solutes in heterogeneous groundwater systems: self-
        organization, entropy, work, Hydrol. Earth Syst. Sci., 25, 5337–5353, https://doi.org/10.5194/hess-25-5337-2021, 2021.

Zhao, J., Wang, D., Yang, H., and Sivapalan, M.: Unifying catchment water balance models for different time scales through the maximum
        entropy production principle, Water Resour. Res., 52, 7503–7512, https://doi.org/10.1002/2016WR018977, 2016.